High-resolution Precipitation Monitoring with a Dense Seismic Nodal Array

J. Hua[1]*†, M. Wu[2]†, J. P. Mulholland[3], J. D. Neelin[4], V. C. Tsai[5], D. T. Trugman[6]

[1] Department of Geological Sciences, Jackson School of Geosciences, The University of Texas at Austin; Austin, TX, 78712 USA.

[2] Joint Institute for Regional Earth System Science and Engineering, University of California, Los Angeles, Los Angeles, CA, 90095 USA.

[3] Department of Atmospheric Sciences, John D. Odegard School of Aerospace Sciences, The University of North Dakota, Grand Forks, ND, 58202 USA.

[4] Department of Atmospheric and Oceanic Sciences, University of California, Los Angeles, Los Angeles, CA, 90095 USA.

[5] Department of Earth, Environmental and Planetary Sciences, Brown University, Providence, RI, 02912 USA.

[6] Nevada Seismological Laboratory, University of Nevada, Reno, Reno, NV, 89557 USA.

Corresponding author: Junlin Hua (jhua0610@gmail.com)

† These authors contributed equally to this work

Key Points:

- We develop a method for detailed monitoring of surface precipitation using dense seismic arrays.
- Seismic monitoring offers higher spatial and temporal resolution than traditional precipitation monitoring methods.
- Seismic precipitation signals can be used to detect and characterize hailstorms.

Abstract

Accurate precipitation monitoring is crucial for understanding climate change and rainfall-driven hazards at a local scale. However, the current suite of monitoring approaches have different insufficiencies, including low spatial and temporal resolutions, and the inability to monitor potentially destructive precipitation events such as hailstorms. In this study, we develop an array-based solution to monitor rainfall with seismic nodal stations, offering both high spatial and high temporal resolutions. We analyze seismic records from densely spaced, high-frequency seismometers in Oklahoma, and identify signals from all 9 precipitation events that occurred during the one-month station deployment in 2016. After removing anthropogenic noise and Earth structure response, the obtained precipitation spatial pattern mimics the one from an operational weather radar, while offering higher spatial and temporal resolutions. We further show the potential of this approach to monitor hail with joint analysis of seismic intensity and independent precipitation rate measurements, and advocate for coordinated seismological-meteorological field campaign design.

Plain Language Summary

Accurate rainfall monitoring plays a key role in natural hazard assessment. However, current monitoring approaches provide limited spatial (e.g., sparsely located rain gauges) or temporal information (e.g., weather radar products available every 5 minutes but not more frequently). Therefore, to supplement these existing approaches, a new technique that can cover a large area and update frequently is required. In this study, we found that weak ground vibrations caused by raindrop impacts, recorded by densely deployed instruments that measure earthquake-generated waves, can fulfill this requirement. We examined such rainfall ground vibration data in part of

Oklahoma in 2016, and found that the new technique successfully retrieved detailed rainfall information. Additionally, besides the amount of rainfall, the new technique could also provide information on the size of raindrops or hailstones hitting the ground, making it a potential tool for monitoring hail, which is now largely based on manual reporting.

1 Introduction

Accurate monitoring of precipitation is essential to our understanding of the water and energy cycles, and can inform rainfall-driven hazard mitigation. Surface precipitation can be used to infer information about atmospheric water vapor, convection and latent heating, and it is a key input for terrestrial ecological and hydrological modeling (Arnold et al., 1998; Fodor & Kovács, 2005). Regarding hazards, extreme precipitation can cause mass movements including landslides and debris flows (Chen et al., 2015), and produce flash floods when the precipitation rate is beyond the infiltration capacity (Cheremisinoff, 1998). Furthermore, long-term observational precipitation data facilitate studies of climate change (Trenberth, 2011), which can have highly variable impacts at local scales.

Among these precipitation-related hazards, hailfall is known to cause severe economic damage and bodily injury. Hail often brings significant losses in both urban areas and farmland (T. M. Brown et al., 2015; Roberts & Vasudevan, 2015). One recorded hailstorm in 1995 injured 109 people during an outdoor festival (*Storm Data - May 1995*, 1995), and hailstorms may even cause deaths. Therefore, accurate real-time quantification of the areal extent and intensity of hailfall is highly relevant for hazard mitigation.

Currently, precipitation is usually monitored in two ways: 1) direct measurement on the ground, or 2) remote sensing of hydrometeors (i.e., liquid and solid water particles in the air).

Automatic direct measurement of surface rainfall is most commonly conducted using catching-type rain gauges, such as tipping-bucket gauges which are globally employed in weather stations (L. G. Lanza et al., 2022). The instrument sensitivity depends on the bucket size (typically ~0.2 mm) and the integration time between buckets depends on the precipitation intensity (Marsalek, 1981). Hence, when the precipitation rate is low, timely precipitation updates are not available, and when the precipitation is high, the gauge underestimates precipitation during emptying periods (Marsalek, 1981). Meanwhile, low-cost tipping-bucket gauges are not designed to measure droplet sizes. Unlike rain or snow, direct hail measurement still requires much human effort using disposable foam hailpads (Palencia et al., 2009), especially given that hailpad networks need to be dense because of the local character of hailfall (Cifelli et al., 2005; Fraile et al., 2003; Fraile et al., 1991).

Unlike surface measurements which can only sample precipitation from a small areal extent, ground-based and space-borne radar is used to detect precipitation over large areas. In general, radars gain information about hydrometeors in the atmosphere and then estimate precipitation based on empirical relationships between reflectivity and precipitation rate (Fulton et al., 1998; Giangrande & Ryzhkov, 2008), forward modeling of attenuation by hydrometeors (Iguchi, 2020), or the shapes of raindrops measured by orthogonally polarized echoes (Seliga & Bringi, 1976). However, while offering good spatial coverage, depending on the instruments and platforms, the temporal resolution of typical radar precipitation products is longer, ranging from min to hours, and satellite radar precipitation products have a lower kilometer-scale spatial resolution.

Recent advancements in understanding seismic precipitation signals (Bakker et al., 2022; Dean, 2017; Rindraharisaona et al., 2022) provide an alternative to counter these weaknesses of existing precipitation monitoring approaches by using seismic waves, which are generated when raindrops impact the ground and excite waves, at frequencies typically above 50 Hz (Bakker et al., 2022; Dean, 2017; Rindraharisaona et al., 2022) for nearby raindrop impacts. Hence, unlike remotely-sensed radar measurements, the seismic intensity serves as a direct sampling of surface precipitation similar to rain gauges with high temporal resolution. Meanwhile, compared to traditional tipping-bucket rain gauges, the seismic intensity is dependent on the weight and speed of each raindrop in addition to the overall precipitation rate (Bakker et al., 2022; Dean, 2017; Rindraharisaona et al., 2022), making it sensitive to the precipitation type and the hydrometeor size, and thus could potentially be used to detect hail. Because a single seismic station is sensitive only to raindrops that fall within ~10 m of it (Bakker et al., 2022), a seismic array is required to monitor regional rainfall patterns.

Oklahoma is a perfect place to test the proposed seismic array precipitation monitoring approach. The climate in Oklahoma is regulated by low-level warm and moist advection from the Gulf of Mexico and mid-level cold and dry air from Canada and the Rocky Mountains, which bring severe weather to the southern Great Plains. Thunderstorms frequently occur between April and October, peaking in May and June, and are often accompanied by tornadoes and large hail (R. M. Brown, 1991). A low-level jet stream flows from the Gulf of Mexico through parts of Oklahoma, overlapping with locations that experience the most severe weather (Bonner, 1968). Central and North Central Oklahoma display two precipitation peaks throughout the year, namely in May and September (R. M. Brown, 1991).

Between 14 April 2016 and 10 May 2016, 1833 high-frequency seismic nodal stations from the LArge-n Seismic Survey in Oklahoma (LASSO) experiment were deployed with nominal station spacing of ~400 m along county roads in Grant County, Oklahoma (Figure 1), for a study region about 25 km by 32 km, and the stations were buried in ~18 cm deep shallow holes with ~3 cm soil cover (Dougherty et al., 2019). Such shallow burial depths enable the following detection of rainfall signals (Rindraharisaona et al., 2022). This experiment was initially designed to study the induced seismicity around the region (Cochran et al., 2020). During the deployment period, there were nine precipitation events in the same region, and these precipitation events pertain to different storm types (Table S1), including disorganized "pulse-type" thunderstorms, supercell thunderstorms, and mesoscale convective systems with scattered instances of large hail, making it an ideal dataset to test the seismic precipitation monitoring approach.

In this study, we extracted seismic precipitation signals from all LASSO stations. We then solved the two main challenges for array-based monitoring: 1) removing anthropogenic noise, and 2) accounting for differences in Earth structure response between stations. With these corrections, seismic-estimated precipitation intensities from the array are compared with measurements from a local tipping-bucket rain gauge at a Department of Energy (DOE) Atmospheric Radiation Measurement (ARM) external facility and a nearby WSR-88D S-band ground-based operational weather radar at Vance Air Force Base, Oklahoma (Figure 1), to test the resolution of this new approach. In addition to seismic-only precipitation rate retrievals, we also performed a joint analysis of seismic intensities and radar precipitation rate products to test the potential use for hail detection.

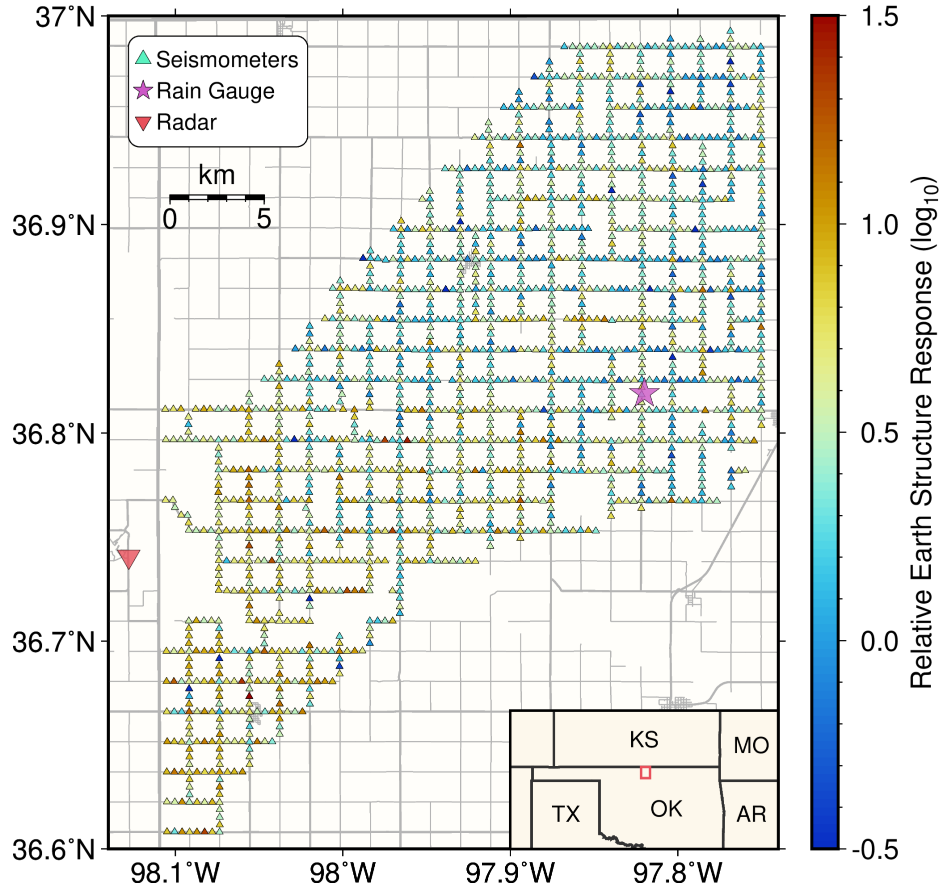

Figure 1. Map of the study area. Triangles show individual seismic nodal stations, color coded by the relative Earth structure response with respect to the reference station (Network: 2A, Station: 340, location shown in Figure S1). The inverted red triangle and the magenta star mark locations for the ground-based radar and the rain gauge. Gray lines are roads. The study area is outlined by the red box in the map at the bottom right corner.

2 Materials and Methods

2.1 Seismic-derived precipitation signal and its physical meaning

Based on satellite and radar data for the study area, nine precipitation events occurred during the deployment period and within the footprint of the array (with each event containing multiple sub-events). Seismograms from the LASSO arrays were requested for all these events, and we obtained seismic displacement data from 1825 individual stations (Figure 1) (data lost for 8 stations).

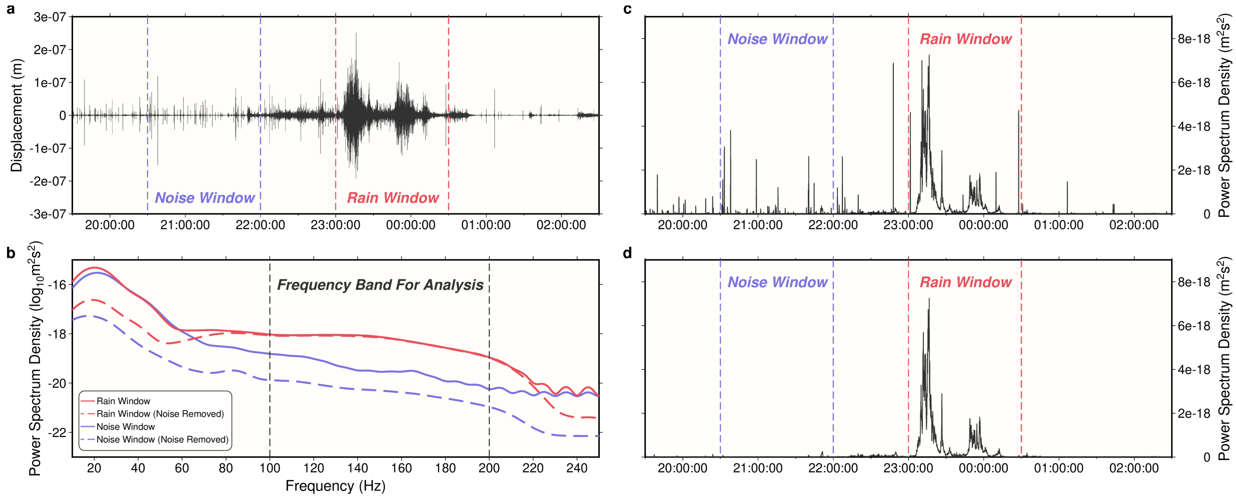

Figure 2. Seismic precipitation signals. (a) Displacement seismogram for a precipitation event on 19 April 2016 sampled by Station: 150 (black line), filtered at 100-200 Hz. Rain window (red) and noise window (blue) for following analyses are divided by dashed lines. (b) Averaged power spectral density for the rain window (red) and noise window (blue) in (a). Solid lines show original PSD, dashed lines show denoised PSD. The frequency range between 100 and 200 Hz is less affected by noise. (c)/(d) Averaged seismic power spectral density between 100 and 200 Hz before/after removing anthropogenic noises. Times used in this study are all in UTC.

Based on the seismograms, a much higher level of background ‘tremor’ is observed during precipitation events (e.g., Figure 2a), and these elevated tremor records are hereafter referred to as seismic precipitation signals. Power spectral densities (PSDs) were calculated for every second between 10 Hz (the corner frequency of the nodal instruments) and 250 Hz (Nyquist frequency) using the Welch method (Welch, 1967) (Text S2 in Supporting Information S1). The Welch method calculates the overall PSD around ±5 s, making the effective time resolution of the PSD 1-10 s. Comparing seismic PSDs for time windows with and without the precipitation, seismic power at frequencies over 60 Hz is greater during precipitation (Figure 2b), as observed in previous studies (Bakker et al., 2022; Dean, 2017; Rindraharisaona et al., 2022).

These elevated seismic PSDs during precipitation events are caused by hydrometeors hitting the ground (Bakker et al., 2022; Dean, 2017). As the seismic precipitation signal is due to the combination of seismic waves from all impact events between hydrometeors and the ground, the impact induced seismic ground motion can be modeled similarly to stochastic bedload impacts (Bakker et al., 2022; Tsai et al., 2012), and the recorded displacement spectrum $u_i(f)$ at station i at a distance of r can be characterized as

$$u_i(f) = F_j(f)G_i(f,r), \qquad F_j(f) = m_j v_j e^{-i2\pi f t_j}, \tag{1}$$

where $F_j(f)$ is the force of the impact (Fourier transform of $m_j v_j \delta(t-t_j)$, δ the Dirac delta function), and m_j, v_j, and t_j are the mass, fall speed and impact time of a single hydrometeor particle j. $G_i(f,r)$ is the displacement Green's function which represents the response of Earth structure (meanings for all used symbols summarized in Table S2). This expression is valid when the impact is instantaneous, and the particle does not rebound. Assuming impacts happen randomly in space, the PSD of the displacement seismogram $PSD_i(f)$ is expressed as:

$$PSD_i(f) = \left|NF^2(f)\right|\int_0^\infty 2\pi r G_i^2(f,r)dr = Nm^2v^2\int_0^\infty 2\pi r G_i^2(f,r)dr = 2\rho_w \cdot PR_i \cdot E_i \cdot S_i, \tag{2}$$

where N is the number of impacts per area per time (Tsai et al., 2012); m is the particle mass; and v is the particle terminal speed. Nm is equivalent to the particle density (ρ_w) multiplied by the precipitation rate PR, and $0.5mv^2$ to the kinetic energy of a hydrometeor particle (E), and S represents the remaining Earth structure response. Here, eq. (2) is a simplified approximation valid when all particles have the same mass and fall speed. The full derivation for how seismic PSD is related to precipitation rate and kinetic energy when considering the particle size distribution as a normalized Gamma distribution (Testud et al., 2001) is available in Text S1 in Supporting Information S1, and the relationship is similar to eq. (2). Therefore, an elevated PSD could indicate increases in either the precipitation rate or the size of hydrometeors, as the kinetic energy of hydrometeors increases with their sizes. This formulation thus lays the foundation to monitor both regular precipitation events and hailfall (often with higher fall speeds and thus kinetic energy) using seismic data analysis.

2.2 Removing anthropogenic noise and Earth structure response

Based on this quantitative framework, we use the average seismic PSD between 100 and 200 Hz (Figure 2b) to characterize precipitation strength (Figure 2c). This frequency band is selected as it is above 60 Hz, where nearby precipitation starts to dominate the observed tremor, and below 220 Hz, where signals become very weak (Figure 2b). The band is also higher than the main anthropogenic noise window (Rindraharisaona et al., 2022) (4-80 Hz), river noise window (Bakker et al., 2022) (<100 Hz) and where wind noise may dominates (Rindraharisaona et al., 2022) (<70 Hz). Meanwhile, this band is selected to be above the corner frequency of all influential earthquakes (Kemna et al., 2020; Trugman et al., 2021). As expected, consistently high PSD amplitudes are observed during precipitation, but occasional high PSD pulses also occur in intervals without rain (Figure 2c).

Non-precipitation PSD pulses were removed based on their common features. Since the nodal stations were often deployed along roads, the majority of these pulses are short duration traffic signals and are easily removed (Figure 2c). Compared with precipitation signals, these anthropogenic pulses are also particularly strong at low frequencies (Rindraharisaona et al., 2022) (<80 Hz, Figure 2b). Based on these two characteristics, denoising criteria were designed to find and remove this anthropogenic noise (Text S2 in Supporting Information S1). After denoising, most pulses were successfully removed (Figure 2d), and as expected, seismic PSDs during non-precipitation intervals are significantly reduced and now two orders of magnitude lower than during precipitation intervals (Figure 2b). We found denoising only marginally reduces the 100-200 Hz PSD during precipitation (Figure 2b).

In order to analyze signals from different stations systematically, their different Earth structure responses (Dean, 2017; Rindraharisaona et al., 2022) must be corrected. Based on eq. (2), the difference in log-scale for seismic PSD from two stations *i* and *k* is expressed as

$$\log\frac{PSD_i}{PSD_k}=\log\frac{PR_i\cdot E_i\cdot S_i}{PR_k\cdot E_k\cdot S_k}=\left(\log PR_i\cdot E_i-\log PR_k\cdot E_k\right)+\left(\log S_i-\log S_k\right). \tag{3}$$

The first part on the right-hand side of eq. (3) corresponds to differences in rain intensity between stations, and the second part corresponds to their difference in Earth structure response. To quantify the Earth structure response, we first measured this seismic PSD difference ($\log(PSD_i/PSD_k)$) at station pairs that are within 1.5 km apart for each shared precipitation window (Text S3 in Supporting Information S1), and calculated their average. Because only close station pairs were used, their overall precipitation intensity is similar. Therefore, after averaging, the first part on the right-hand side of eq. (3) is eliminated, with only the Earth structure difference left (second part of the right-hand side in eq. 3). With this, we set the response at a reference station to be one (Station 340), and solved for the optimal relative Earth structure response *R* at each station to minimize an L_2-norm cost function that is similar to $\left\|\log\left(PSD_i/PSD_k\right)-\log\left(R_i/R_k\right)\right\|_2$ (eq. S14 in Supporting Information S1). This optimization problem has an explicit and constant Hessian, so those relative responses *R* can be directly obtained using Newton's method (Galántai, 2000) (Figures 1 & S1a), with their standard deviations provided by the inverse Hessian (Thacker, 1989) (Figure S1b). More details about the optimization are available in Text S3 in Supporting Information S1.

The relative structure response at different stations shows two orders of magnitude differences (Figure 1), indicating a substantial difference in burial depth or soil type (Rindraharisaona et al., 2022), and emphasizing the importance of this correction. However, the low standard deviation (Figure S1b) for the solved responses ensures the accuracy after correction. Interestingly, we also found the resolved structure response broadly similar to the spatial pattern of high-frequency seismic ground motion due to teleseismic waves (Chang et al., 2021), again indicating the influence of near surface lithology on the amplitude of seismic records. In the following analyses, seismic PSDs are divided by their relative Earth structure response R.

3 Results

3.1 Monitoring precipitation with seismic data

Seismic power spectral densities at each location are then calculated by weighted average seismic PSDs from nearby stations (Text S4 in Supporting Information S1). To compare seismic-derived precipitation signals with other precipitation measurements, we first obtained the averaged PSD at the location of a tipping-bucket rain gauge (Figure 1). The seismic-derived precipitation estimates clearly show elevated PSDs during precipitation periods (Figures 3a & S2). An example is shown for the precipitation event on 17 April 2016, which consisted of five sub-events over ~12 hours (Figure 3a).

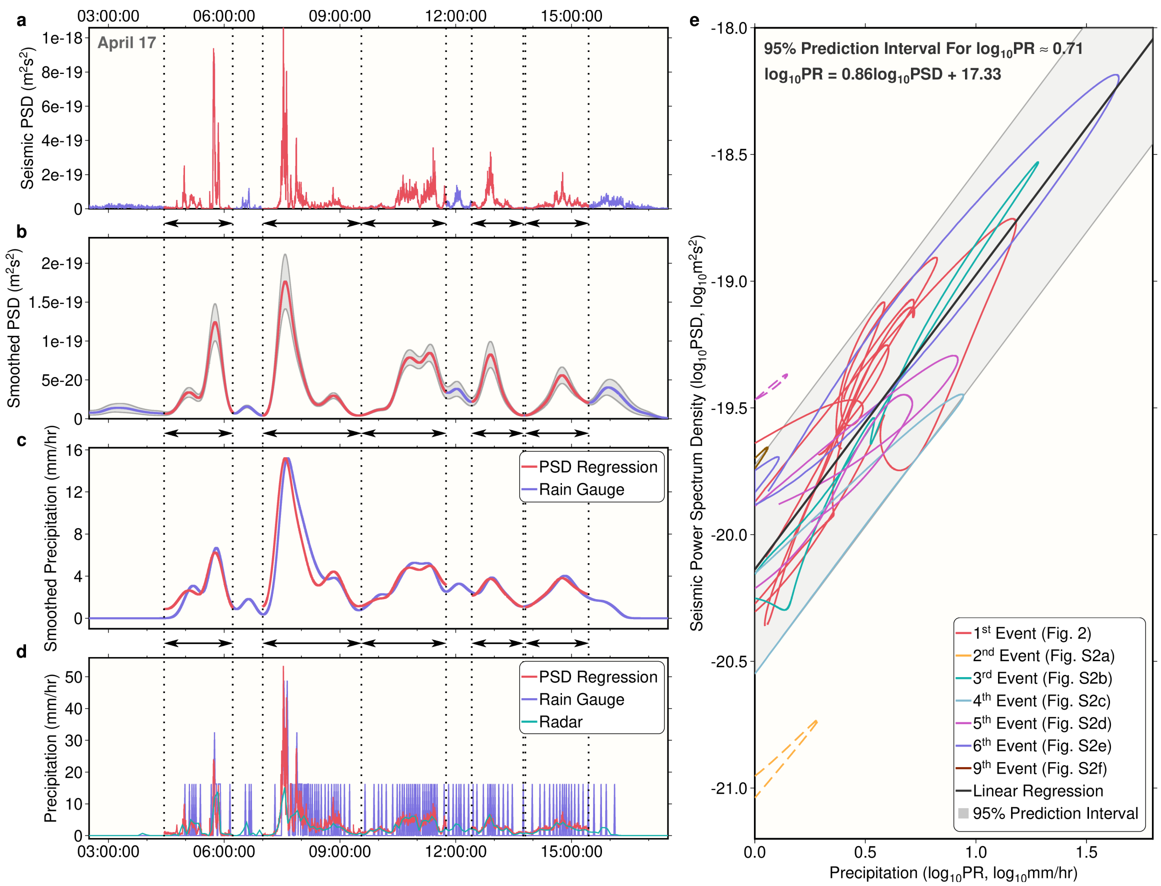

Figure 3. Seismic precipitation measurements in comparison with rain gauge. (a) Seismic power spectral density at the location of the rain gauge for a precipitation event on 17 April 2016. The profile is obtained by the weighted average seismic PSD sampled at several nearby stations. Red sections mark five individual precipitation sub-events, and are divided by black dotted lines. (b) Similar to (a), but is smoothed. The gray shadow shows one standard deviation due to station averaging. All smoothing for panels in this Figure is done by convolving a Gaussian (10 min half-width). (c) The blue line shows smoothed precipitation rate from the rain gauge. Red sections are converted precipitation rate from seismic PSD by fitting each red PSD sections in (b) to the rain gauge measurements in (c) through linear regression after both are converted to log-scales. (d) The blue line shows raw rain gauge records, which often appear discretized due to its integration time. Red lines show converted precipitation rate using the unsmoothed PSD in (a) and the regression relationship in (c). The green line shows instantaneous precipitation rate from the ground-based radar. (e) Smoothed seismic PSD versus smoothed rain gauge precipitation rate in log-scale. Different colors for events on different days (Figure S1, each event may consist of multiple sub-events as separated lines). The black line shows the fitted linear relationship between the PSD and the precipitation rate using all sub-events except two dashed line outliers, and the 95% prediction interval for the fitting is characterized by the gray shadow. Fitted relationship and the 95% interval width are shown at the top left corner.

The seismic-derived signal for this event is compared with precipitation rate from the rain gauge. Because the integration time of the rain gauge between bucket tips can be longer than one minute (the measurement interval) when the rain rate is low, the precipitation record is not continuous (Figures 3d & S2). Hence, for comparison, both seismic PSD and rain gauge precipitation rates were smoothed by convolving a 10-min half width Gaussian (Figure 3b-c), and it is shown that both timing and relative strength were comparable between the two measurements for those precipitation sub-events.

To estimate the precipitation rate using seismic PSDs, we derived their conversion relationships. Based on eq. (2), in log-scale, the seismic PSD (log*PSD*) varies linearly with the precipitation rate (log*PR*). For each sub-event, we obtained parameters to convert seismic PSD linearly to precipitation rate using the ordinary least-square method (Text S5 in Supporting Information S1), and a close fit is reached (Figures 3c & S2). These conversion parameters were then applied to the unsmoothed PSD as well (Figure 3a). Compared with precipitation rates from the rain gauge and the nearby operational weather radar (Figure 1), seismic PSD-derived precipitation rates offer better temporal resolution (Figures 3d & S2).

The overall conversion relationship between seismic PSD and precipitation rate is also calculated in the same manner using data from all events (Text S5 in Supporting Information S1). Based on this relationship (Figure 3e), the *PSD* is linearly related to $PR^{1.16}$, indicating a dependence of raindrop kinetic energy on the precipitation rate (eq. 2). This dependence is weaker than that from a previous study (Bakker et al., 2022), potentially due to differences in the type of precipitating weather systems. The prediction interval of the relationship is relatively wide (Figure 3e), suggesting raindrop kinetic energy varies between events. In particular, the first sub-event on 26 April 2016 (Figure S2d) shows abnormally higher seismic PSD relative to the contemporary precipitation (Figure 3e), indicating much larger kinetic energy for the falling raindrops or ice particles (i.e., hail). Another abnormal event is on 18 April 2016 where the PSD is very low.

We then generated seismic precipitation maps for the entire region using the same method by weighted averaging seismic PSDs from nearby stations (Text S4 in Supporting Information S1). These maps are compared with instantaneous precipitation rate retrieved from a nearby operational ground-based weather radar, whose close distance (Figure 1) ensures a lateral resolution as high as ~300 m over the area (angular resolution of 1°). In general, precipitation patterns are similar (e.g., Figures 4 & S3) between the two measurements, but seismic maps show much higher temporal resolution (Movies S1-S9). Seismic maps also show narrower precipitation regions than the radar (e.g. Figures 4a versus b), suggesting a higher effective spatial resolution.

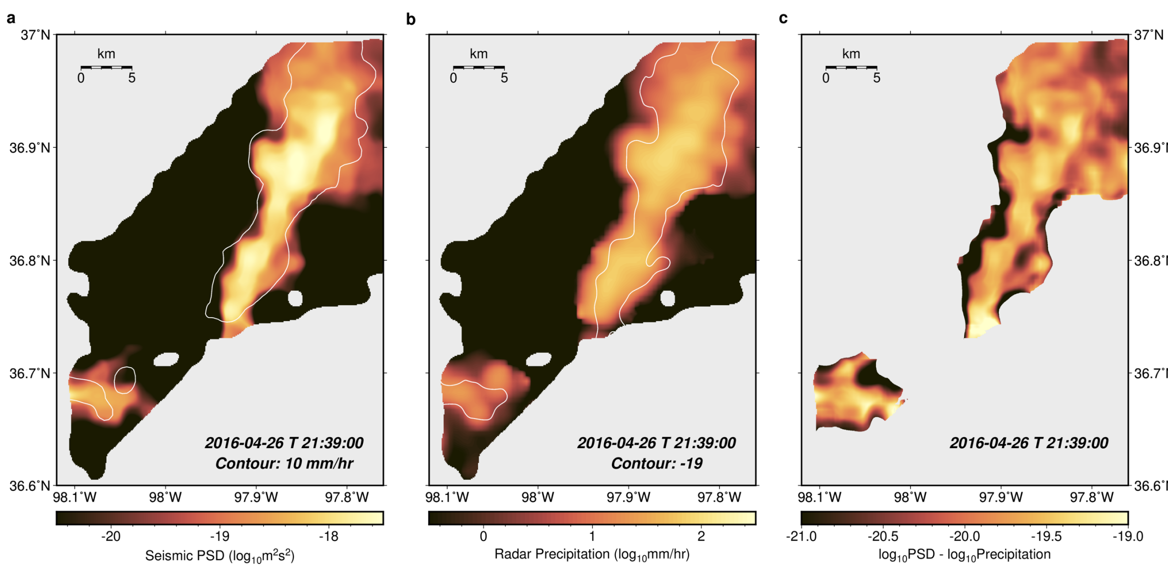

Figure 4. Precipitation spatial distribution. (a)/(b) Maps in log-scale for the seismic power spectral density / radar instantaneous precipitation rate at 21:39:00 UTC, 26 April 2016. The white line in (a) shows the contour for 10 mm hr^{-1} radar precipitation in (b), and the white line in (b) shows the contour for 10^{-19} m^2 s^2 seismic PSD in (a), which is equivalent to 10 mm hr^{-1} precipitation rate if using the relationship in Figure 3e. Regions with low data coverage are shown in gray. (c) The seismic PSD map in (a) subtracting the radar precipitation map in (b) (PSD-PR difference). Only regions with both radar precipitation rate and seismic converted precipitation rate (Figure 3e) higher than 0.3 mm hr^{-1} are plotted. The variable plotted in (c) is expected to be proportional to the kinetic energy of a raindrop.

4.2 Hail detection through joint analyses of seismic and precipitation measurements

Seismic signals are sensitive to the particle kinetic energy, so hailfall can potentially be monitored by combining seismic PSD with independent precipitation rate measurements. Based on eq. (2), the difference between the PSD and the precipitation rate (hereafter referred to as the PSD-PR difference), defined as log*PSD*-log*PR*, is proportional to the particle kinetic energy (log*E*). Therefore, the difference between a seismic PSD map and an independent precipitation rate map (here we use instantaneous precipitation from radar measurements) would indicate the kinetic energy of hydrometeors (Figure 4c, Movies S1-S9).

Such PSD-PR differences are compared with the probability of hail of any size (POH) and the maximum expected hail size (MEHS) estimated from the ground-based radar (Figures 5 & S4). These radar hail parameters are generated by the WSR-88D radar's Hail Detection Algorithm based on large reflectivity values above the freezing level, and are available for individual storm cells, with storm cell center locations also given (Witt et al., 1998). Here, we only consider hail parameters from storm cells whose centers are less than 500 m away from precipitating locations (both radar and seismic PSD indicates a precipitation rate higher than 0.3 mm/hr, using the relationship in Figure 3e to convert PSD to precipitation). Human reports are also considered when their minimum distance to the array are less than 10 km (Figures 5 & S4). It is shown that larger PSD-PR difference occurs when POH and MEHS are greater. For example, from 20:30 to 22:00 UTC on 26 April 2016, such differences increase along with increases in POH and MEHS (Figure 5), consistent with the abnormally high seismic PSD converted precipitation rate using the overall relationship in Figure 3e (Figure 5a). Overall, when POH is higher than 80%, the PSD-PR difference is systematically higher than the case when POH is zero (Figure 5b), suggesting the potential to detect hail using a seismic array, and compared with these hail indices, our seismic approach is likely to map the spatial distribution of hailfall within a storm cell.

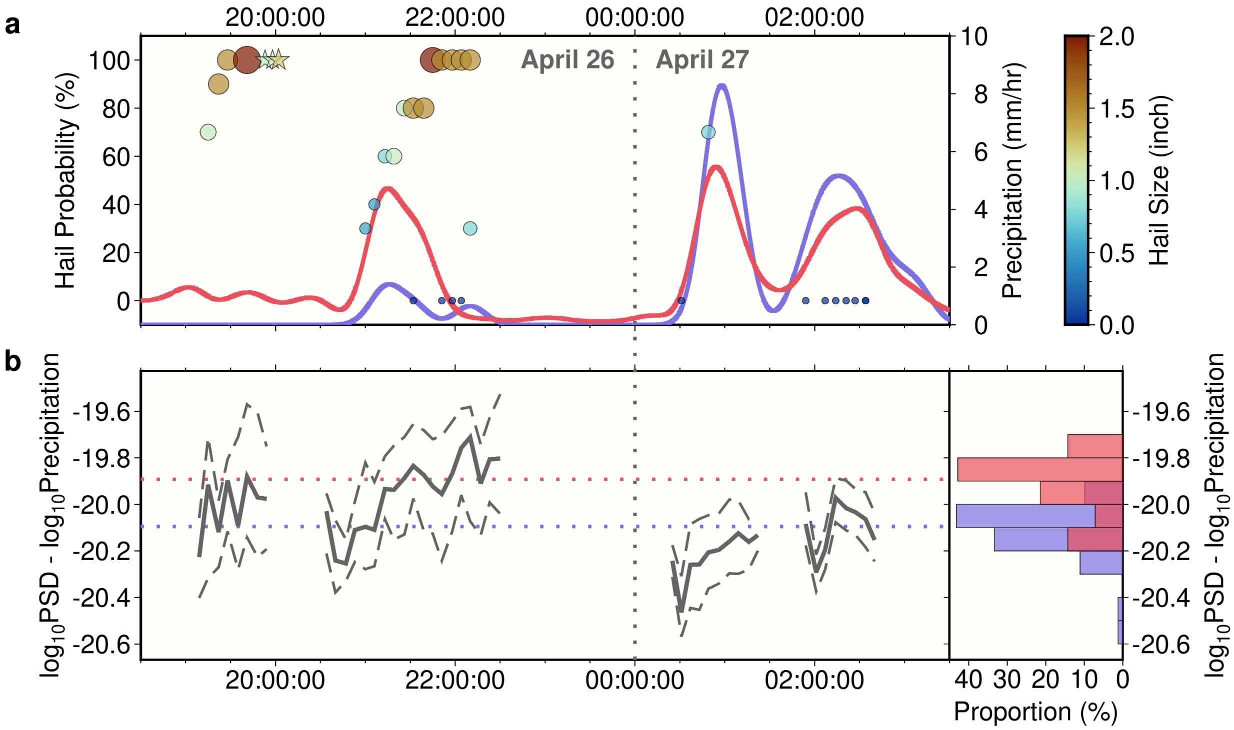

Figure 5. The relationship between seismic PSD and hailfalls. (a) Similar to Figure 3c, the blue line shows the smoothed rain gauge precipitation rate for the event on 26 April 2016, and the red line shows the smoothed seismic PSD converted precipitation rate using the relationship in Figure 3e. A clear overestimation appears at around 21:15:00 UTC. Circles show the probability of hail of any size (POH) estimated from the ground-based weather radar, and both their sizes and colors show the maximum expected hail size (MEHS). These hail related parameters are only plotted when their corresponding storm cell location is less than 0.5 km from the closest place with rainfall (over 0.3 mm hr^{-1} precipitation rate indicated by both the radar and the seismic PSD relationship in Figure 3e). Times with multiple nearby storm cells may show multiple circles. Stars show hail reports (treated as POH 100%) that are less than 10 km from the closest seismic station, with colors showing the reported hail size. The storm cell before 20:00:00 UTC did not pass the rain gauge (Movie S5). (b) The left panel shows the PSD-PR difference when the total precipitating areas are larger than 20 km^2. Solid line shows the median value for the precipitating area, while dashed lines show 25^{th} and 75^{th} percentiles. The right panel shows histograms for the median of this difference (solid line in the left panel) for all events (Figure S4). Red bars are collected at times when POH is greater than 80%, and blues bars are collected when POH is zero. Median values for these two histograms are plotted as dotted lines in the left panel.

4 Discussion

Though our seismic-derived precipitation estimates infer precipitation indirectly through droplet impact, they show strong potential to complement existing monitoring approaches by leveraging five distinct advantages: 1) extremely high temporal resolution (1-10 s); 2) very high spatial resolution (~500 m); 3) sensitivity to raindrop or hailstone sizes; 4) influence only from precipitation reaching the ground; and 5) wider spatial sampling extent compared to rain gauges.

The time resolution of seismic precipitation signals is higher than traditional approaches to precipitation monitoring. For instance, the operational weather radar used in this study offers instantaneous precipitation rate not more frequent than every 5 min due to its scanning strategy (Movies S1-S9) and is not always accurate (Figures 3d & 2), while precipitation accumulation without gauge-radar bias is only available in an hourly manner (Fulton et al., 1998). Meanwhile, tipping bucket rain gauge measurements are often not continuous (e.g., Figure 3d). Satellite precipitation products also usually have a lower time resolution from min to hours. In contrast, the seismic signals are analyzed at a much higher frequency (100-200 Hz), resulting in a temporal resolution on the order of seconds in this study.

Seismic monitoring also offers higher spatial resolution. Compared with operational weather radar, seismic surface measurements reveal narrower precipitation areas (Figures 4 & S3, Movies S1-S9). Moreover, although radar products offer precipitation rates at high nominal spatial resolution (e.g. Figures S3c, f), raw radar data often contains abrupt changes between neighboring locations partly due to oversampling during data retrieval, and the revealed precipitation region from these unsmoothed data is in general still broader than the surface seismic measurement (Figure S3). Spatial resolutions of precipitation estimates from space-borne radars are even lower, on the order of kilometers (Maggioni et al., 2016). For a tipping-bucket rain gauge system deployed as part of a dense array, it would have an apparent high spatial resolution, but the effective resolution is restricted by its temporal resolution. For a rain gauge with the instrument sensitivity of 0.2 mm, if the precipitation rate is 1 mm hr^{-1}, the rain gauge could only record precipitation every 12 min, which would translate into a spatial resolution of 4 km if the precipitating feature travels at a speed of 20 km hr^{-1}.

Another unique feature of the seismic measurement is its sensitivity to particle sizes (eq. 2). Currently, to directly measure raindrop or hailstone sizes, a high-cost disdrometer (L. Lanza & Vuerich, 2012) or a hand-operated hailpad (Palencia et al., 2009) is required. For actual hail monitoring, common practices depend on human reports, labor-intensive hailpad network (Cifelli et al., 2005; Fraile et al., 2003), or hail information retrieved from weather radars which depend on calibration from the relatively limited number of hailpad measurements (Mezzasalma et al., 2000) and often mismatch the location from hail reports (Brook et al., 2021). In contrast, the seismic PSD itself strongly depends on the hydrometeor kinetic energy (Bakker et al., 2022; Dean, 2017; Rindraharisaona et al., 2022) (eq. 2), which is evident when PSDs are compared with rain gauge precipitation rates (Figure 5a). The computed PSD-PR differences are broadly consistent with radar-based hail indices (Figure 5b), showing the capability of hail monitoring when independent seismic and precipitation measurements are available. Such hail detection capability points to the usefulness of designing collaborative observational programs between seismology and meteorology communities. Specifically, during future deployments of high-density seismic nodal arrays, a coordinated meteorological field campaign with the deployment of disdrometers and hailpad arrays would help unveil the seismic characteristics of hailstones at different sizes and move towards a multidisciplinary real-time product of hail detection and characterization.

Moreover, seismic precipitation monitoring also benefits from its surface measurement nature and a larger spatial extent of sampling. Compared with ground-based and space-borne radars, which remotely sense hydrometeors in the air, seismic signals are generated by actual raindrops hitting the ground (Bakker et al., 2022; Dean, 2017). Particularly for the potential usage in hail detection, a ground-based radar is prone to bias aloft due to strong attenuation during a convective storm (Féral et al., 2003), and it can only produce hail data in a probabilistic sense, which in contrast, are not problems for the seismic surface measurement. Meanwhile, assuming precipitation seismic signals are mainly Rayleigh waves (Sánchez-Sesma et al., 2011; Tsai et al., 2012), the seismic PSD is sensitive to combined impacts from raindrops within ~5-25 m (Bakker et al., 2022), much wider than the areal extent sampled by rain gauges, ensuring a continuous precipitation measurement and avoiding random errors due to infrequent raindrop sampling over a small area.

Further improvements could be made to the seismic monitoring approach. 1) The Earth structure response has a different frequency dependence for various soil types and burial depths (Dean, 2017; Rindraharisaona et al., 2022), so it could be better corrected in a frequency-dependent way, which could be easily adjusted based on the method in this study. 2) Thunder signals (Zhu & Stensrud, 2019) are not fully removed during denoising (e.g., Movie S1). 3) While rain signals are found up to 450 Hz (Dean, 2017; Roth et al., 2016), LASSO seismic stations cannot resolve signals over 250 Hz, and its data quality is problematic above 200 Hz (Figure 2b), suggesting better instrumentation would improve the monitoring. 4) The size distribution and the fall speed of hailstones would likely differ from those of raindrops. Hence, more experiments are required to better understand seismic hail signals. 5) Theoretically, at higher frequencies, the precipitation seismic PSD would be greater but only from raindrops falling within shorter distances to the station (Bakker et al., 2022), which indicates for different precipitation events, the optimal frequency band could be different, e.g., regular precipitation events could benefit from higher frequencies due to potentially easier PSD discrimination, but sparsely distributed hail may require lower frequencies for the measurement to be robust.

With these special characters of seismic monitoring, though only deployed for one-month, interesting meteorological phenomena were revealed. For example, a discrete supercell thunderstorm tracked northeastward over the domain with a relatively narrow, yet intense swath of high-precipitation rates and associated accumulation between around 21:30:00 UTC and 22:30:00 UTC on 9 May (Movie S9). The improved spatial and temporal resolution of the surface seismic monitoring measurements are exemplified in a comparison between the seismic converted one-hour precipitation accumulation and the radar one-hour precipitation accumulation—the seismic converted one-hour precipitation accumulation shows a more detailed and higher precipitation accumulation swath compared to the radar one-hour precipitation accumulation swath for the supercell thunderstorm. Other similar examples include between around 16:30:00 UTC and 17:00:00 UTC on 29 April (Movie S6) and between around 16:00:00 UTC and 16:30:00 UTC on 8 May (Movie S7). This pattern not only was present with isolated storm modes, but also was apparent with linear bands of thunderstorms, such as between around 21:00:00 UTC and 22:30:00 UTC on 26 April (Movie S5).

5 Conclusions

In this study, we demonstrate that seismic array analysis has the potential to become a strong complement to existing precipitation monitoring approaches with the experimental practices. After removing anthropogenic noises and relative Earth structural responses, the seismic approach can successfully retrieve surface precipitation patterns at very high spatial and temporal resolutions. Meanwhile, as seismic intensity depends not only on the precipitation rate but also on the kinetic energy of hydrometeors, this new approach has a unique sensitivity to raindrop and hailstone sizes, which makes it possible to monitor hail occurrences when combined with independent precipitation rate data.

Acknowledgments

We thank D. Wang for help regarding the use of ARM data. We thank M. Wiederspahn for data management. We thank S. P. Grand and E. Sandvol for discussions.

Open Research

All LASSO seismic data used in this study sampled between 17 April 2016 and 10 April 2016 were downloaded from the IRIS DMC (http://ds.iris.edu/ds/nodes/dmc/) with the network code of 2A. WSR-88D radar products at the Vance Air Force Base (KVNX), including Digital Accumulation Array (DAA), Digital Instantaneous Precipitation Rate (DPR) and Hail Index (HI), were obtained through NOAA's Weather and Climate Toolkit (https://www.ncdc.noaa.gov/wct/index.php). Tipping-bucket rain gauge data and impact disdrometer data were from the E32 site and the C1 site, respectively, of the DOE ARM Southern Great Plains atmospheric observatory (https://www.arm.gov/capabilities/observatories/sgp/locations/). Hail reports were obtained from

NOAA's Storm Prediction Center Severe Weather Events Archive (https://www.spc.noaa.gov/exper/archive/events/). Satellite precipitation estimates shown in Movies were from the NOAA Climate Prediction Center Morphing Technique (https://www.cpc.ncep.noaa.gov/products/janowiak/cmorph_description.html). All computer codes used for data processing, analysis, and plotting are available upon request.

Conflict of Interest Statement

The authors have no conflict of interest to declare.

References

Arnold, J. G., Srinivasan, R., Muttiah, R. S., & Williams, J. R. (1998). Large area hydrologic modeling and assessment part I: model development 1. *JAWRA Journal of the American Water Resources Association, 34*(1), 73-89.

Bakker, M., Legout, C., Gimbert, F., Nord, G., Boudevillain, B., & Freche, G. (2022). Seismic modelling and observations of rainfall. *Journal of Hydrology, 610*, 127812.

Bonner, W. D. (1968). Climatology of the low level jet. *Monthly Weather Review, 96*(12), 833-850.

Brook, J. P., Protat, A., Soderholm, J., Carlin, J. T., McGowan, H., & Warren, R. A. (2021). HailTrack—Improving radar-based hailfall estimates by modeling hail trajectories. *Journal of applied meteorology and climatology, 60*(3), 237-254.

Brown, R. M. (1991). *A climatic guide for North Central Oklahoma*. Retrieved from

Brown, T. M., Pogorzelski, W. H., & Giammanco, I. M. (2015). Evaluating hail damage using property insurance claims data. *Weather, Climate, and Society, 7*(3), 197-210.

Chang, H., Abercrombie, R., Nakata, N., Pennington, C., Kemna, K., Cochran, E., & Harrington, R. (2021). Quantifying earthquake source parameter uncertainties associated with local site effects using a dense array.

Chen, C.-W., Saito, H., & Oguchi, T. (2015). Rainfall intensity–duration conditions for mass movements in Taiwan. *Progress in Earth and Planetary Science, 2*(1), 1-13.

Cheremisinoff, N. P. (1998). *Groundwater remediation and treatment technologies*: Elsevier.

Cifelli, R., Doesken, N., Kennedy, P., Carey, L. D., Rutledge, S. A., Gimmestad, C., & Depue, T. (2005). The community collaborative rain, hail, and snow network: Informal education for scientists and citizens. *Bulletin of the American Meteorological Society, 86*(8), 1069-1077.

Cochran, E. S., Wickham-Piotrowski, A., Kemna, K. B., Harrington, R. M., Dougherty, S. L., & Castro, A. F. P. (2020). Minimal clustering of injection-induced earthquakes observed with a large-n seismic array. *Bulletin of the Seismological Society of America, 110*(5), 2005-2017.

Dean, T. (2017). The seismic signature of rain. *Geophysics, 82*(5), P53-P60.

Dougherty, S. L., Cochran, E. S., & Harrington, R. M. (2019). The Large-N seismic survey in Oklahoma (LASSO) experiment. *Seismological Research Letters, 90*(5), 2051-2057.

Féral, L., Sauvageot, H., & Soula, S. (2003). Hail detection using S-and C-band radar reflectivity difference. *Journal of Atmospheric and oceanic technology, 20*(2), 233-248.

Fodor, N., & Kovács, G. J. (2005). Sensitivity of crop models to the inaccuracy of meteorological observations. *Physics and Chemistry of the Earth, Parts A/B/C, 30*(1-3), 53-57.

Fraile, R., Berthet, C., Dessens, J., & Sánchez, J. L. (2003). Return periods of severe hailfalls computed from hailpad data. *Atmospheric research, 67*, 189-202.

Fraile, R., Sánchez, J. L., de la Madrid, J. L., & Castro, A. (1991). A network of hailpads in Spain. *The Journal of Weather Modification, 23*(1), 56-62.

Fulton, R. A., Breidenbach, J. P., Seo, D.-J., Miller, D. A., & O'Bannon, T. (1998). The WSR-88D rainfall algorithm. *Weather and forecasting, 13*(2), 377-395.

Galántai, A. (2000). The theory of Newton's method. *Journal of Computational and Applied Mathematics, 124*(1-2), 25-44.

Giangrande, S. E., & Ryzhkov, A. V. (2008). Estimation of rainfall based on the results of polarimetric echo classification. *Journal of applied meteorology and climatology, 47*(9), 2445-2462.

Gunn, R., & Kinzer, G. D. (1949). The terminal velocity of fall for water droplets in stagnant air. *Journal of Atmospheric Sciences, 6*(4), 243-248.

Iguchi, T. (2020). Dual-frequency precipitation radar (DPR) on the global precipitation measurement (GPM) mission's core observatory. In *Satellite precipitation measurement* (pp. 183-192): Springer.

Kemna, K., Peña Castro, A., Harrington, R., & Cochran, E. S. (2020). Using a large-n seismic array to explore the robustness of spectral estimations. *Geophysical Research Letters, 47*(21), e2020GL089342.

Lanza, L., & Vuerich, E. (2012). Non-parametric analysis of one-minute rain intensity measurements from the WMO Field Intercomparison. *Atmospheric research, 103*, 52-59.

Lanza, L. G., Cauteruccio, A., & Stagnaro, M. (2022). Rain gauge measurements. In *Rainfall* (pp. 77-108): Elsevier.

Maggioni, V., Meyers, P. C., & Robinson, M. D. (2016). A review of merged high-resolution satellite precipitation product accuracy during the Tropical Rainfall Measuring Mission (TRMM) era. *Journal of Hydrometeorology, 17*(4), 1101-1117.

Marsalek, J. (1981). Calibration of the tipping-bucket raingage. *Journal of Hydrology, 53*(3-4), 343-354.

Marshall, J. S., & Palmer, W. M. (1948). The distribution of raindrops with size. *J. meteor., 5*, 165-166.

Mezzasalma, P., Nanni, S., & Alberoni, P. (2000). Performance of a Hdr-based hail detection algorithm in Northern Italy. *Physics and Chemistry of the Earth, Part B: Hydrology, Oceans and Atmosphere, 25*(10-12), 949-952.

Palencia, C., Castro, A., Giaiotti, D., Stel, F., Vinet, F., & Fraile, R. (2009). Hailpad-based research: A bibliometric review. *Atmospheric research, 93*(1-3), 664-670.

Rindraharisaona, E., Réchou, A., Fontaine, F., Barruol, G., Stamenoff, P., Boudevillain, B., et al. (2022). Seismic signature of rain and wind inferred from seismic data. *Earth and Space Science*, e2022EA002328.

Roberts, M. E., & Vasudevan, S. (2015). *Fine-grained multi-factor hail damage modelling.* Paper presented at the 2015 Conference on Technologies and Applications of Artificial Intelligence (TAAI).

Rogers, R. R. (1989). Raindrop Collision Rates. *Journal of Atmospheric Sciences, 46*(15), 2469-2472. 10.1175/1520-0469(1989)046<2469:RCR>2.0.CO;2

Roth, D. L., Brodsky, E. E., Finnegan, N. J., Rickenmann, D., Turowski, J. M., & Badoux, A. (2016). Bed load sediment transport inferred from seismic signals near a river. *Journal of Geophysical Research: Earth Surface, 121*(4), 725-747.

Sánchez-Sesma, F. J., Weaver, R. L., Kawase, H., Matsushima, S., Luzón, F., & Campillo, M. (2011). Energy partitions among elastic waves for dynamic surface loads in a semi-infinite solid. *Bulletin of the Seismological Society of America, 101*(4), 1704-1709.

Seliga, T. A., & Bringi, V. (1976). Potential use of radar differential reflectivity measurements at orthogonal polarizations for measuring precipitation. *Journal of applied meteorology and climatology, 15*(1), 69-76.

Storm Data - May 1995. (1995). (G. W. Goodge Ed. Vol. 37). National Climatic Data Center.

Testud, J., Oury, S., Black, R. A., Amayenc, P., & Dou, X. (2001). The concept of "normalized" distribution to describe raindrop spectra: A tool for cloud physics and cloud remote sensing. *Journal of Applied Meteorology, 40*(6), 1118-1140.

Thacker, W. C. (1989). The role of the Hessian matrix in fitting models to measurements. *Journal of Geophysical Research: Oceans, 94*(C5), 6177-6196.

Trenberth, K. E. (2011). Changes in precipitation with climate change. *Climate research, 47*(1-2), 123-138.

Trugman, D. T., Chu, S. X., & Tsai, V. C. (2021). Earthquake Source Complexity Controls the Frequency Dependence of Near-Source Radiation Patterns. *Geophysical Research Letters, 48*(17), e2021GL095022.

Tsai, V. C., Minchew, B., Lamb, M. P., & Ampuero, J. P. (2012). A physical model for seismic noise generation from sediment transport in rivers. *Geophysical Research Letters, 39*(2).

Welch, P. (1967). The use of fast Fourier transform for the estimation of power spectra: a method based on time averaging over short, modified periodograms. *IEEE Transactions on audio and electroacoustics, 15*(2), 70-73.

Witt, A., Eilts, M. D., Stumpf, G. J., Johnson, J., Mitchell, E. D. W., & Thomas, K. W. (1998). An enhanced hail detection algorithm for the WSR-88D. *Weather and forecasting, 13*(2), 286-303.

Yau, M. K., & Rogers, R. R. (1996). *A short course in cloud physics*: Elsevier.

Zhu, T., & Stensrud, D. J. (2019). Characterizing thunder-induced ground motions using fiber-optic distributed acoustic sensing array. *Journal of Geophysical Research: Atmospheres, 124*(23), 12810-12823.